

Exploring Intrinsic and Extrinsic p -type Dopability of Atomically Thin β -TeO₂ from First Principles

Rafael Costa-Amaral,[†] Soungmin Bae,[†] Vu Thi Ngoc Huyen,[†] and Yu Kumagai^{*,†}

[†]*Institute for Materials Research, Tohoku University, Sendai 980-8577, Japan.*

[‡]*Organization for Advanced Studies, Tohoku University, Sendai 980-8577, Japan*

E-mail: yukumagai@tohoku.ac.jp

Abstract

Two-dimensional (2D) β -TeO₂ has gained attention as a promising material for optoelectronic and power device applications, thanks to its transparency and high hole mobility. However, the underlying mechanism behind its p -type conductivity and dopability remains unclear. In this study, we investigate the intrinsic and extrinsic point defects in monolayer and bilayer β -TeO₂, the latter of which has been experimentally synthesized, using the HSE+D3 hybrid functional. Our results reveal that most intrinsic defects are unlikely to contribute to p -type doping in 2D β -TeO₂. Moreover, Si contamination could further impair p -type conductivity. Since the point defects do not contribute to p -type conductivity, we propose two possible mechanisms for hole conduction: hopping conduction via localized impurity states, and substrate effects. We also explored substitutional p -type doping in 2D β -TeO₂ with 10 trivalent elements. Among these, the Bi dopant is found to exhibit a relatively shallow acceptor transition level. However, most dopants tend to introduce deep localized states, where hole polarons become trapped at Te's lone pairs. Interestingly, monolayer β -TeO₂ shows potential advantages over bilayers due to reduced self-compensation effects for p -type

dopants. These findings provide valuable insights into defect engineering strategies for future electronic applications involving 2D β -TeO₂.

1 Introduction

Wide band gap semiconductors have been extensively used in high-frequency and high-voltage applications, serving as fundamental components for ultraviolet light emitters, power electronics, optoelectronics, and radio-frequency devices.^{1,2} The fabrication of n -type oxide semiconductors has achieved remarkable success with high electron mobility and efficiency, such as in Al-doped ZnO,³ Sn-doped In₂O₃,⁴ and amorphous IGZO.⁵ However, the lack of p -type counterparts with comparable performance limits the potential for complementary metal-oxide-semiconductor technology and bipolar junction transistors, essential components for high-efficiency power devices and integrated circuits, although numerous computational efforts have been made to identify superior transparent conducting oxides.⁶⁻⁸

Two-dimensional (2D) β -TeO₂ has captured significant attention as a potential high-mobility p -type semiconductor. Calculations based on the density-functional theory first predicted high hole mobility of β -TeO₂.⁹ Zavabeti *et al.* subsequently synthesized atomically thin β -TeO₂ on SiO₂ substrates.¹⁰ These nanosheets exhibit a direct band gap of 3.66 eV and high hole mobility at room temperature, which provides new possibilities for device applications, especially for field-effect transistors (FETs). These results have attracted increasing attention to tellurium oxides, with several studies reporting experimental and theoretical observations of TeO₂.¹¹⁻¹⁶

While the p -type conductivity in 2D β -TeO₂ is observed even without external doping, the main origin of the p -type conductivity in 2D β -TeO₂ still remains unexplored. Point defects such as intrinsic vacancies and unintentional dopants are known sources of hole carriers in semiconductors.^{17,18} Although they are expected to play crucial roles in hole conduction in 2D β -TeO₂, this hypothesis has not been verified experimentally and theoretically. Previously,

we have reported on the calculations of point defects and impurities in the *bulk* β -TeO₂,¹⁹ and found that no intrinsic defects contribute to hole conductivity. This raises the question whether they would contribute to the *p*-type conductivity when the dimensionality is reduced.

Thus, our aim is to uncover the origins of *p*-type conductivity in atomically thin β -TeO₂ by calculating point defects, including unintentional dopants, using a hybrid functional that reproduces the experimental band gap. We primarily target the bilayer β -TeO₂ because the synthesized 2D β -TeO₂ is composed of the bilayer in experiments.¹⁰ Additionally, we also focus on the monolayer to investigate the thickness effect. As a result, we reveal that neither native defects nor Se and Si impurities contribute to meaningful hole concentration. To explain the experimentally observed *p*-type conductivity, we also discuss the substrate effect by demonstrating charge transfer from quartz substrate to 2D β -TeO₂. Finally, for applications such as photodetectors and solar cells, where controlling hole concentration is crucial, we investigate potential acceptor dopants from 10 elements capable of adopting a trivalent oxidation state at the Te sites.

2 Results and Discussion

2.1 Unit-cell parameters

Prior to studying point defects in 2D TeO₂, we benchmarked several exchange-correlation functionals including PBE,²⁰ PBEsol,²¹ SCAN,²² SCAN0,²³ PBE0,²⁴ HSE06,^{25,26} HSEsol,²⁷ and HSE06 with the D3 Van der Waals correction²⁸ (HSE+D3), in predicting the structural properties and the band gap of the bilayer β -TeO₂. The in-plane lattice constants and their ratio (a and b , b/a), the Te-Te interlayer distance, Δz_{Te} (see Fig. 1(a)), and the band gap E_g are summarized in Table 1. While the PBE functional overestimates both in-plane lattice parameters, PBEsol markedly underestimates a , leading to a larger b/a ratio. As anticipated, both functionals underestimate the experimental band gap of 3.66 eV measured by Scanning Tunneling Spectroscopy (STS) on the nanosheet.¹⁰ The SCAN functional yields

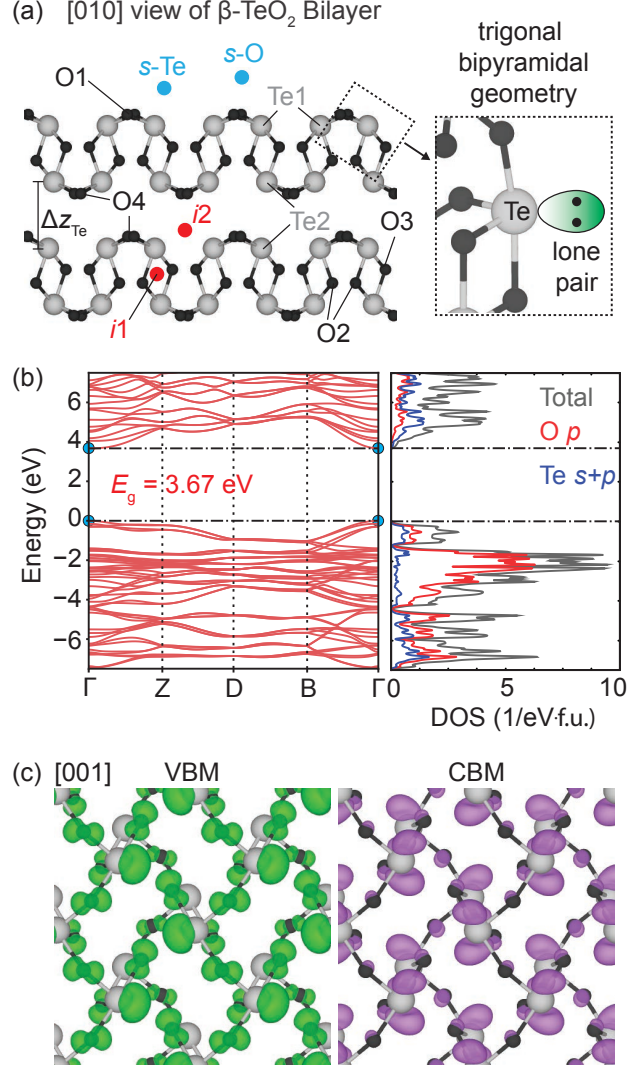


Figure 1: (a) Side view of the optimized β -TeO₂ bilayer, where the Te and O atoms are gray and black, respectively. The nonequivalent Te and O sites are labeled accordingly along with the surface sites, s -Te, and s -O, in blue, and the interstitial sites, $i1$, and $i2$, in red. A close up image of the structure depicts the Te coordinated to four O atoms in a distorted trigonal bipyramidal geometry. The schematic of the Te- $5sp$ lone pair orbital oriented toward the vacant space is also illustrated. (b) The band structure and density of states of the β -TeO₂ bilayer calculated with the HSE+D3 functional. The energy along the y -axis is shown relative to the VBM. The dash-dotted lines represent the energy zero and the CBM, while the circles mark the VBM and CBM positions that are located at the Γ point. (c) The partial charge densities of the VBM and CBM in the β -TeO₂ bilayer viewed from the [001] direction. The isosurface levels are set to $0.0005 e/\text{Bohr}^3$.

better results than PBE and PBEsol but still underestimates the band gap by 1 eV. Screened HSE functionals (HSE06 and HSEsol), predict the band gap to be, respectively, 3.74 eV and

3.51 eV, much closer to the experiment.¹⁰ The addition of dispersion corrections²⁸ with the HSE06 functional (HSE+D3) reduces the interlayer spacing from 3.44 Å to 3.34 Å, and yields the b/a ratio and band gap (3.67 eV) closer to the experimental values. On the other hand, unscreened hybrid functionals (PBE0 and SCAN0) largely overestimates the band gap of the β -TeO₂ bilayer, giving values of 4.44 eV and 5.37 eV. Consequently, the HSE+D3 functional was selected to investigate the point defect properties in 2D β -TeO₂, as it most accurately reproduces experimental parameters.

Table 1: In-plane lattice constants, a and b , the b/a ratio, the Te-Te interlayer distance, Δz_{Te} shown in Figure 1, and the band gap, E_g , of the β -TeO₂ bilayer obtained from different exchange-correlation functionals. For both a and b , the relative errors are also provided. The HSE+D3 functional is shown in **bold** as it is adopted for the point-defect calculations.

xc functional	a (Å)	Error (%)	b (Å)	Error (%)	b/a	Δz_{Te} (Å)	E_g (eV)
PBE	5.55	1.54	5.74	2.37	1.04	3.34	2.46
PBEsol	5.23	-4.19	5.69	1.46	1.09	3.14	2.23
SCAN	5.34	-2.27	5.62	0.18	1.05	3.30	2.68
HSE06	5.50	0.75	5.60	-0.16	1.02	3.44	3.74
HSEsol	5.25	-4.00	5.58	-0.43	1.06	3.26	3.51
HSE+D3	5.41	-0.93	5.60	-0.14	1.03	3.34	3.67
SCAN0	5.36	-1.90	5.53	-1.39	1.03	3.33	5.37
PBE0	5.48	0.37	5.58	-0.42	1.02	3.44	4.44
Expt. ^{10,29}	5.46	—	5.61	—	1.03	—	3.66

In Figure 1b, we show the band structure and density of states (DOS) for the bilayer; the monolayer results are found in Figure S1 in the *Supporting Information*. A slightly larger band gap of 3.92 eV is observed for the monolayer, aligning with a previous report.⁹ From the DOS, a strong hybridization between the Te and O states is found at the valence band maximum (VBM) and conduction band minimum (CBM), which is also related with their spatial distribution shown in Figure 1c. The VBM, where carrier holes propagate, primarily consists of Te-5*sp* lone pairs and O-2*p* orbitals. This delocalization may contribute to the high hole mobility observed in the bilayer β -TeO₂.^{9,10}

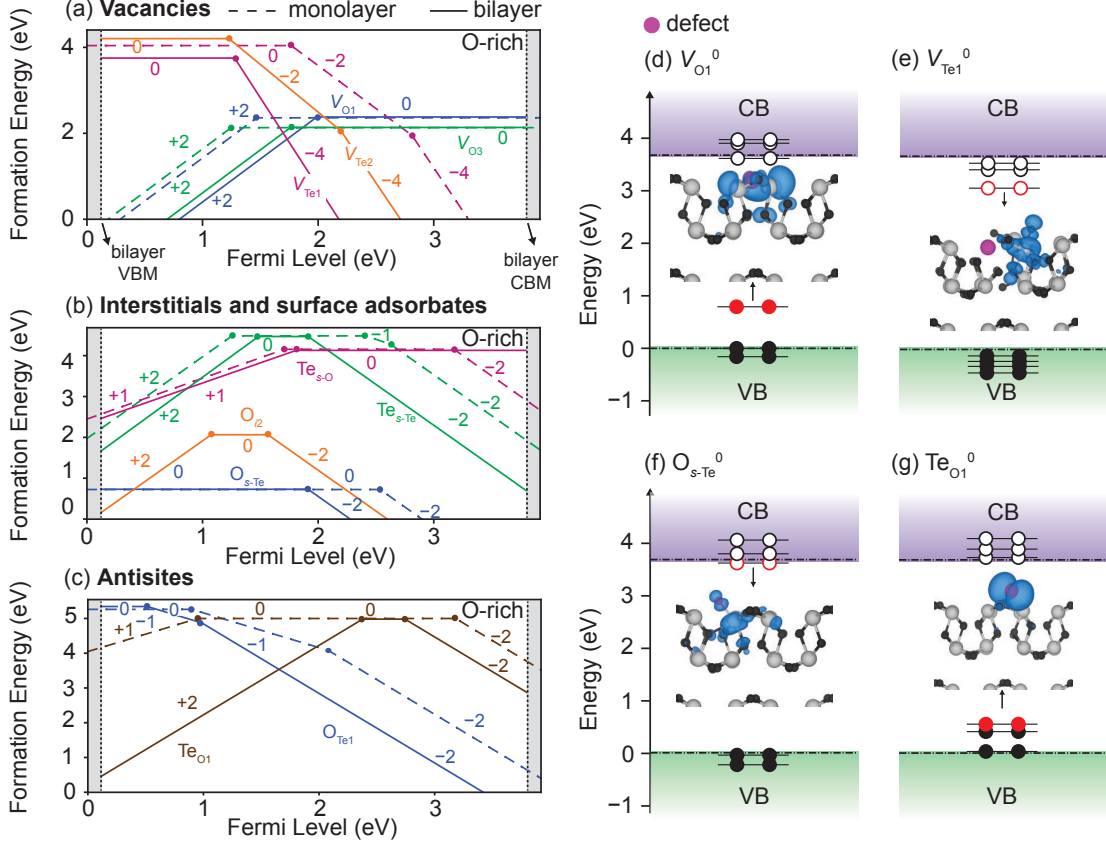


Figure 2: (a–c) Formation energies of the (a) vacancies, (b) interstitials and surface adsorbates, and (c) antisites as a function of the Fermi level. The chemical potentials are set at the O-rich condition. The dashed and solid lines represent results for the monolayer and bilayer, respectively. The Fermi levels are referenced to the VBM of the monolayer (see text for details). (d–g) Single particle levels of V_{O1}^0 , V_{Te1}^0 , O_{s-Te}^0 , and Te_{O1}^0 in the β -TeO₂ bilayer. The blue isosurfaces correspond to the squared wave functions labeled with red circles at $0.005 e/\text{Bohr}^3$.

2.2 Intrinsic defects and unintentional dopants

Next, the point defects in the monolayer and bilayer β -TeO₂ are explored with the HSE+D3 functional. In this study, several nonequivalent sites are considered, as illustrated in Figures 1 and S1 in the *Supporting Information*. The monolayer contains one Te site and two nonequivalent O sites, located in the outer and inner oxygen layers, and they are labeled as Te1, O1, and O2, respectively. In the bilayer, the number of nonequivalent sites doubles because atoms can be located either on the surface side or between the layers. Consequently, additional sites Te2, O3, and O4, along with a new interstitial site between the two layers

(see Figure 1a), are introduced.

The formation energies under the O-rich condition for the lowest energy defects of each type, *i.e.*, vacancies, interstitials, surface adsorbates, and antisites, are shown in Figure 2a–c. In this study, the band edges between the monolayer and bilayer are aligned at the vacuum level. We begin our discussion with the intrinsic vacancies (V_{Te} and V_{O}) in Figure 2a. Since PBEsol predicts nearly degenerate formation energies for V_{O} at all four oxygen sites, we selectively calculated O1 and O3 using HSE+D3. They present very deep donor levels; the V_{O} in the bilayer has a (+2/0) transition level around 1.66 and 1.88 eV, while that in the monolayer is about 1.25 and 1.47 eV above their respective VBMs. The electrons at the in-gap states in the neutral charge states are captured by neighboring Te atoms, as illustrated in Figure 2d.

Even under the O-rich (Te-poor) conditions, V_{Te}^0 exhibits relatively high formation energies, around 4 eV in the bilayer. Here, superscripts in defect notations represent charge states. This is expected, as forming a Te vacancy requires breaking four Te–O bonds, compared to two bonds for an O vacancy. The formation energy of V_{Te1}^0 is 0.5 eV lower than that of V_{Te2}^0 , indicating that V_{Te} preferentially forms on the vacuum-facing side. As shown in Figure 2e, the unoccupied defect states of V_{Te1}^0 are localized in a nearby TeO_5 cluster. However, these vacancies act as deep acceptors with transition levels at 1.17 eV (1.77 eV) in the bilayer (monolayer), making them unlikely to be a main source of hole carriers in 2D $\beta\text{-TeO}_2$.

Calculation results of interstitials and surface adsorbates are presented in Figure 2b. In the bilayer, O primarily occupies the interstitial region between the layers (i_2), with amphoteric characteristics with transition levels of (+2/0) and (0/−2) at 0.96 eV and 1.57 eV, respectively. For the surface defects, the Te adatoms adsorb preferentially on the O on-top site in the neutral charge states, whereas the Te on-top site becomes more stable in charged states, showing an amphoteric behavior similar to O_{i2} . Under the O-rich condition, O adsorption on top of Te ($O_{s\text{-Te}}$) exhibits a remarkably low formation energy. In analogy

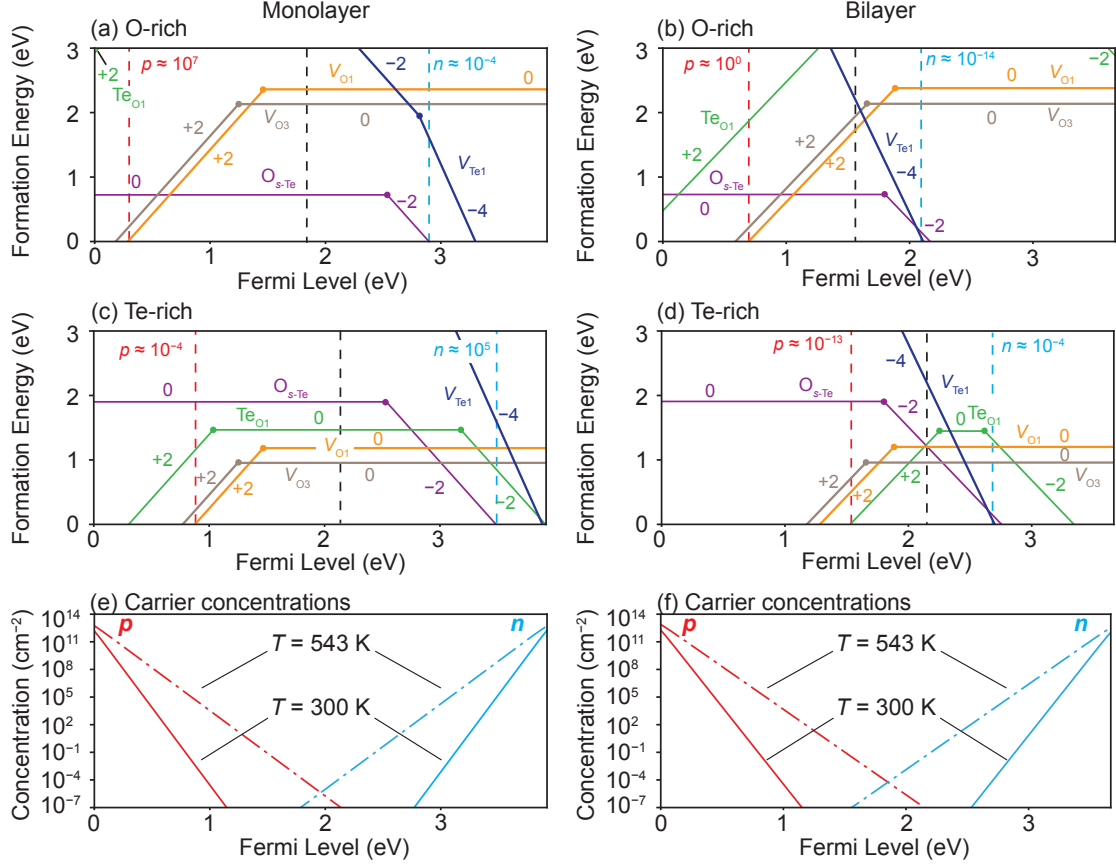


Figure 3: (a–d) Same as Fig. 2(a–c) but focusing on dominant native defects in (a,c) the monolayer and (b, d) the bilayer β -TeO₂ under (a,b) the O-rich and (c, d) the Te-rich conditions. The vertical black dashed lines are the equilibrium Fermi levels at 300 K (see the main text for details). The vertical red and blue dashed lines represent the lower and upper limits of the Fermi levels at which formation energies of the charged defects are zero, respectively. p and n represent the orders of hole and electron concentrations in cm⁻² at 300 K, respectively. (e,f) Carrier concentrations as a function of the Fermi level for (e) the monolayer and (f) the bilayer β -TeO₂. The Fermi levels are referenced to each VBM in the diagrams.

to $V_{\text{Te}1}$ and $V_{\text{Te}2}$, $O_{s\text{-Te}}$ should not be a significant source of hole carriers due to the (0/−2) deep acceptor levels, at 2.54 eV in the monolayer and 1.80 eV in the bilayer, respectively. As shown in Figure 2f, its hole polaronic states exhibit strong localization at the Te lone pair, as with the Te vacancies.

Due to the large difference in the ionic radii between O^{2-} (1.35 Å) and Te^{4+} (0.66 Å),³⁰ the formation of the antisite defects is expected to be energetically unfavorable. This is indeed observed in Figure 2c, in which $O_{\text{Te}1}$ and Te_{O1} show higher formation energies than

the vacancies, interstitials, and surface adsorbates. However, under the Te-rich conditions, the Te_{O1}^0 formation energy largely decreases to 1.5 eV. Te_{O1} exhibits an amphoteric nature, with deep (+2/0) and (0/-2) transition levels at 2.25 eV and 2.62 eV, respectively. Because of its donor-like behavior and low formation energy in the p -type regime, p -type doping may be inhibited under the Te-rich conditions.

In Figure 3, the formation energies of the dominant native defects under the O- and Te-rich conditions are shown. Based on the charge neutrality condition,^{31,32} we evaluated the equilibrium Fermi levels (E_{F}), as well as the defect and carrier concentrations in 2D β - TeO_2 . The temperature is initially set to the reported bilayer growth temperature (543 K),¹⁰ and then quenched to 300 K, maintaining defect concentrations while allowing charge state transitions.

The calculated E_{F} of the monolayer and bilayer are located at 1.78 eV and 1.60 eV from the VBMs, respectively, at the O-rich conditions, where V_{O1}^{2+} and $\text{O}_{\text{s-Te}}^{2-}$ determine the E_{F} , indicating intrinsically insulating characteristics in both the monolayer and bilayer. For instance, the bilayer presents a hole concentration of $3.4 \times 10^{-15} \text{ cm}^{-2}$. Note that the observed hole concentration determined by the Hall measurement is $1.04 \times 10^9 \text{ cm}^{-2}$.¹⁰ The oxygen adatom is one of the few defects that exists in meaningful concentrations, *e.g.*, $1 \times 10^8 \text{ cm}^{-2}$. However, since it remains neutral at the equilibrium Fermi level, it does not contribute to the p -type conductivity. This suggests that native defects in 2D- TeO_2 are unlikely to be the main source of p -type carriers.

The tendencies of the native defects in 2D- TeO_2 are in line with those of *bulk* β - TeO_2 we reported recently,¹⁹ indicating the intrinsic insulating nature in both 2D and 3D β - TeO_2 . The notable difference is the E_{F} , which is located at 0.53 eV in bulk β - TeO_2 , comparatively closer to the VBM. This is because V_{Te}^{4-} has a lower formation energy in the bulk, while O adsorbates regulate the E_{F} in 2D β - TeO_2 . The dimensionality reduction, however, does not contribute to the hole concentrations, which is the key conclusion of this study.

We extend our investigation to unintentional impurities, namely Se and Si because their

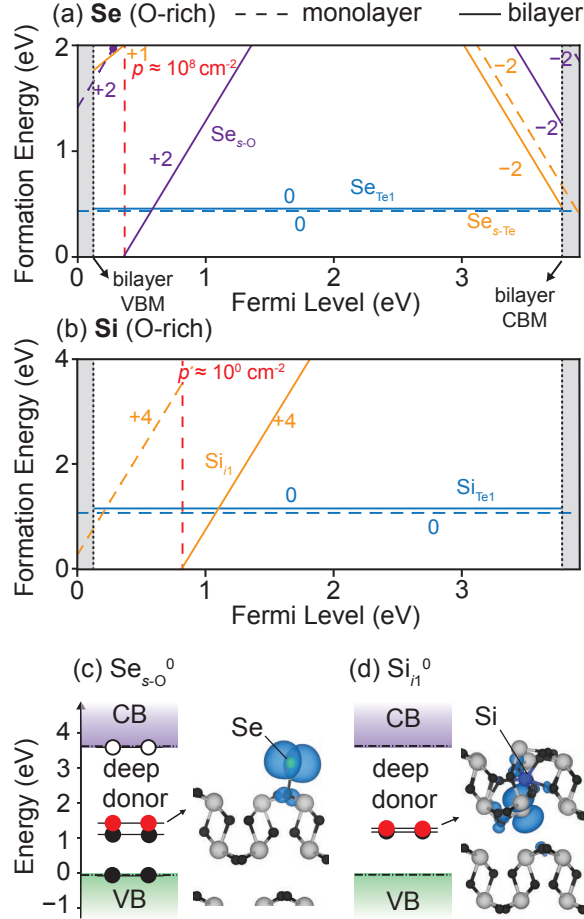


Figure 4: (a,b) Same as Fig. 2(a–c) but for stable substitutional and interstitial defects of the Se and Si impurities under the O-rich conditions. Extended formation energy diagrams are displayed in Figure S6. (c, d) Same as Fig. 2(d–g) but for (c) $\text{Se}_{s-\text{O}}^0$ and (d) Si_{i1}^0 .

presence was confirmed by XPS elemental mapping of the deposited $\beta\text{-TeO}_2$ flakes.¹⁰ Figures 4a and b show the formation energies of Se and Si impurities, respectively. Our calculations show that Se predominantly occupies the substitutional Te sites ($\text{Se}_{\text{Te}1}$), with a formation energy below 0.5 eV. Since Se and Te are in the same group of the periodic table, it is natural that the substitutional defect remains in a neutral charge state. In the bilayer, Se adsorbed on oxygen site ($\text{Se}_{s-\text{O}}$) pins the Fermi level at 0.25 eV above the VBM, which is lower than the pinned level by the oxygen vacancies, resulting in no significant effect. On the other hand, the Si contaminant can efficiently introduce the inner layer interstitial (Si_{i1}^{4+}) at the p -type condition, and therefore, Si should be avoided as much as possible to achieve

the p -type conductivity. As illustrated in Figures 4c and d, both $\text{Se}_{\text{s-O}}^0$ and Si_{i1}^0 defects introduce deep donor states of polaronic nature, which is related to the donor-type behavior.

Based on our calculations, native defects and unintentional dopants do not contribute to the hole conductivity. It is noteworthy that there is a notable mismatch of the Fermi levels observed in 2D β - TeO_2 using the Hall measurement and optical spectra.¹⁰ The Hall measurement estimates hole concentration of the bilayer to be $1.04 \times 10^9 \text{ cm}^{-2}$. Based on our calculated carrier concentrations as a function of the Fermi level (Figure 3f), which can be evaluated from the DOS, this concentration corresponds to the Fermi level around 0.2 eV from the VBM. Meanwhile, the ultraviolet photoelectron spectroscopy (UPS) and STS measurements for the same sample confirm the location of Fermi level at 0.9 eV. This large mismatch suggests that hole conduction is not simply mediated by the VBM or its perturbed states. Instead, we here propose two potential sources for hole conductivity.

The first could be hole propagation through localized defect states. Both experimental and theoretical studies indicate that deep localized defect states are common in 2D materials,³³⁻³⁵ probably due to poor charge carrier screening inherent to their reduced dimensionality.³⁶ This would also be related to the impurity conduction in other 2D materials,^{34,37-39} thus, a similar scenario could occur in 2D β - TeO_2 .

The second possible source is the substrate effect. Charge transfer from the substrate can play a key role, especially in interfaces with 2D materials.⁴⁰⁻⁴² We examined the interaction between β - TeO_2 and the SiO_2 substrate, considering Si-, Si-H-, O-, and O-H-terminated surfaces, which are commonly expected to coexist. Details of the calculations are provided in the *Supporting Information*. Our findings reveal no significant charge transfer at the H-passivated interfaces. However, at Si-rich interfaces, electron transfer to the nanosheet occurs, potentially harming its p -type conductivity. On the other hand, the OH-termination, which is likely to dominate due to water vapor in the environment, promotes charge transfer from the nanosheets to the substrate, potentially enhancing the hole concentration. The -SiO terminations are anticipated to eventually form because the synthesis temperature

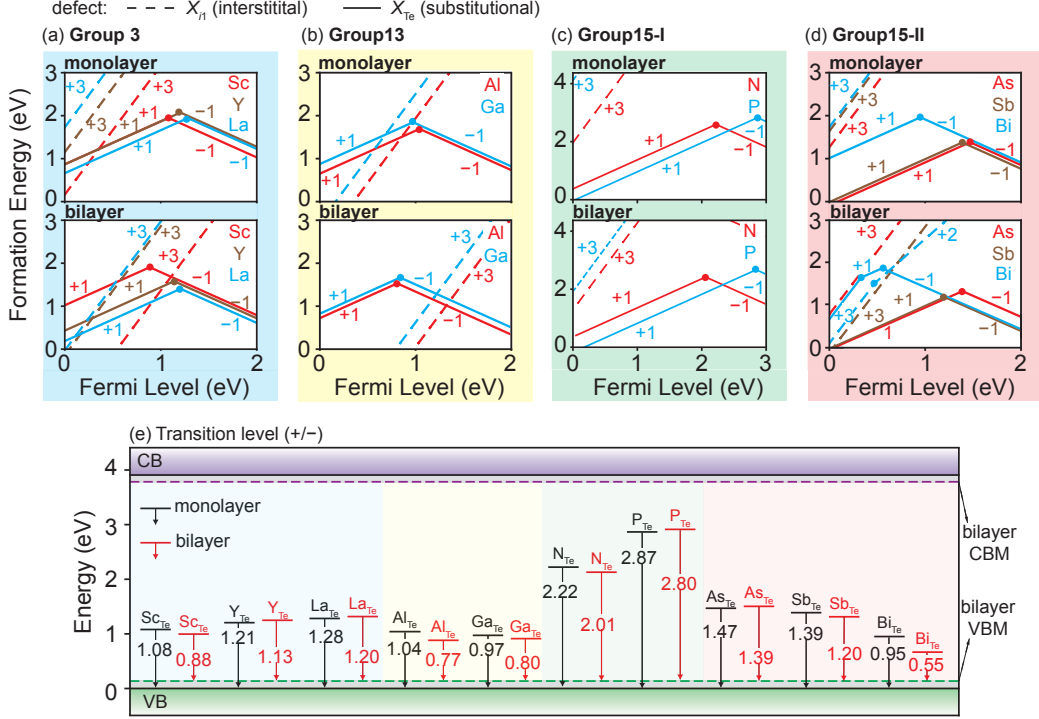


Figure 5: (a–d) Same as Fig. 2(a–c) but focusing on the most stable substitutional and interstitial dopant defects under the O-rich conditions. (e) The (+1/ – 1) transition levels of the substituted dopants.

of the nanosheets exceeds the dehydroxylation threshold for SiO_2 surfaces ($-\text{Si}(\text{OH})_2 \rightarrow -\text{SiO} + \text{H}_2\text{O}$), typically around 200°C .^{43,44} Based on our results, this should further enhance the hole concentration since a 40% increase in charge transfer is observed for a 8% surface coverage of $-\text{SiO}$ terminations. In an extreme scenario, the oxygen-saturated SiO_2 surface, achievable via dry oxidation, removes $4.06 e$ from the 2D $\beta\text{-TeO}_2$ according to the Bader analysis, completely oxidizing some interface Te, which may contribute to the p -type conductivity.

2.3 Screening of acceptor dopants

We then investigated the existence of shallow acceptor dopants in 2D $\beta\text{-TeO}_2$. A total of 10 dopants from groups 3 (Sc, Y, La), 13 (Al, Ga) and 15 (N, P, As, Sb, and Bi) substituting Te sites were calculated.

The defect formation energies and charge transition levels of the interstitials and substitutional impurities at the Te sites (X_{Te}) are presented in Figure 5. For Group 15 elements, we classify them into 15-I (N, P) and 15-II (As, Sb, Bi) because these two classes exhibit distinct behaviors from each other. For the diagrams with extended energy ranges and the other defect types with higher formation energies, refer to Figures S7-10 in the *Supporting Information*. For most dopants, the substitutional sites are the most stable, followed by the interstitial site X_{i1} , which is placed in the layer (see Fig. 1(a)). The only exception is N, which prefers the interlayer space ($i2$ site).

The substitutional X_{Te} defects show direct transitions between -1 and $+1$ charge states, known as the negative- U effect. The effective U value (U^{eff}) between $q-1$, q , $q+1$ is evaluated as

$$U^{\text{eff}}(q - 1/q/q + 1) = E_f[D^{q-1}] + E_f[D^{q+1}] - 2E_f[D^q], \quad (1)$$

where $E_f[D^q]$ is the formation energy of defect D with charge q (see Sec. 4.2). In Table 2, we summarize U^{eff} for the X_{Te} defects, which range from -0.15 to -0.87 eV for the monolayer, and from -0.44 to -1.54 eV for the bilayer.

We also calculated the self-trapped holes (STH) as a polaron ($q = +1$) and a bipolaron ($q = +2$) by placing one and two holes in perfect supercells, respectively, and estimated its U^{eff} . Such STHs are found not to relax to the delocalized states, but their formation energies are unstable over delocalized hole states (see *Supporting Information*). U^{eff} of STHs are -0.22 eV for the monolayer and -0.73 eV for the bilayer, which indicates that the negative U^{eff} observed for the acceptor dopants is related to the intrinsic nature of the bipolarons in 2D β -TeO₂. The instability of the single hole originates from the open-shell $4d^{10}5s^1$ configuration of Te⁵⁺ ions, where a hole is captured. Such valence skipping is often observed in lone pair orbitals. For example, Bi in K-doped XBiO₃ ($X = \text{Ba}, \text{Sr}$) prefers $+3$ and $+5$ oxidation states over the $+4$ state.⁴⁵⁻⁴⁷

Figure 5e displays the $(+1/-1)$ transition levels for the p -type dopants. Group 15-I dopants exhibit particularly deep acceptor levels in both monolayer and bilayer cases, making

them unsuitable candidates for hole doping. For the monolayer, although Ga and Bi are relatively the most promising candidates, their transition levels are still deep. The acceptor states in the bilayer are generally shallower than those in the monolayer. Particularly for Al and Bi dopants, the (+1/−1) transition states shift down to 0.77 eV and 0.55 eV above the VBM, respectively. However, unlike the monolayer, most dopants are self-compensated by X_{i1}^{3+} interstitial defects, significantly limiting the hole dopability of the bilayer. In the bilayer, the defect charge is widely distributed in two layers, leading to a general reduction in Coulomb energy of X_{i1}^{3+} compared to the monolayer, which reduces the formation energies of the interstitials (see Figure S11 for the plane-averaged charge difference). Due to its large ionic size that relates to the reduced self-compensation, Bi remains the most promising dopant candidate for the bilayer.

We acknowledge that Bi still classifies as a deep acceptor, compared to the shallow acceptors in conventional 3D semiconductors, where acceptor transition levels should lie within 0.1 eV above the VBM. As discussed in Sec. 2.2, the hole conductivity may result from hopping through defect bands.^{34,48} If this holds true, doping β -TeO₂ with deep impurities at high concentrations could still enhance *p*-type conductivity, similar to what has been observed in other 2D materials.⁴⁸

3 Conclusions

In this study, we investigated the mechanism of the hole doping observed in 2D β -TeO₂.¹⁰ First, we identified that the HSE+D3 hybrid functional accurately reproduces both the lattice constants and the band gap observed in experiments. We then applied the HSE+D3 functional to study native defects and Se and Si impurities that are unintentionally contaminated in the 2D β -TeO₂. We focused on the monolayer and bilayer β -TeO₂, the latter of which has been experimentally synthesized. Our findings suggest that neither native defects nor unintentional impurities are likely sources of *p*-type conductivity in 2D β -TeO₂. Instead,

Table 2: The effective Hubbard U (U^{eff}), in eV, estimated for the substitutional X_{Te} defects in the monolayer and bilayer of β -TeO₂. The (+1/ - 1) transition levels from the VBM in eV.

dopant	monolayer		bilayer	
	U^{eff}	(+/-) transition	U^{eff}	(+1/ - 1) transition
Sc	-0.26	1.08	-0.90	0.88
Y	-0.30	1.21	-0.44	1.13
La	-0.34	1.28	-0.87	1.20
Al	-0.23	1.04	-0.56	0.77
Ga	-0.15	0.97	-0.61	0.80
N	-0.58	2.22	-1.54	2.13
P	-0.87	2.87	-1.36	2.80
As	-0.34	1.47	-0.56	1.39
Sb	-0.24	1.39	-0.72	1.20
Bi	-0.32	0.95	-0.57	0.55
intrinsic	-0.22	-	-0.73	-

we propose two potential mechanisms for hole conductivity: The first is hole transport through localized defect states, and the second involves substrate effects. We demonstrate the latter using 2D β -TeO₂/SiO₂ interface models, revealing that substrates with OH- and O-rich surfaces may facilitate hole injection into the nanosheets.

Additionally, we investigated 10 elements from groups 3 (Sc, Y, La), 13 (Al, Ga), and 15 (N, P, As, Sb, Bi) as potential external acceptor dopants. All dopants are found to exhibit deep acceptor levels with negative U behavior, with most forming bipolarons bound to neighboring Te-5*sp* lone pairs. Among these, Bi shows the shallowest acceptor level in the bilayer, although the transition levels remain relatively deep. Such doping could promote hole mobility through hopping conduction via localized defect states.^{34,48}

We expect these findings provide valuable understanding of the hole conductivity observed in 2D β -TeO₂ and open new avenues for optimizing its properties for future electronic applications.

4 Computational Details

4.1 First-principles calculations

First-principles calculations were based on the spin-polarized density-functional theory with the projected augmented wave^{49,50} (PAW) method as implemented in the VASP code.⁵¹ For overall calculations, the Heyd-Scuseria-Ernzerhof (HSE06) functional^{25,26} with the DFT-D3 method of Grimme with zero-damping function (HSE+D3) was employed.²⁸ Information on the PAW potentials is found within the *Supporting Information*. To reduce the Pulay stress error, a cutoff energy of 520 eV was used to determine the in-plane lattice parameters of the 2D β -TeO₂ and calculate the competing phases to build the chemical potential diagram (CPD). For the remaining total energy calculations, a cutoff energy of 400 eV was used. The Brillouin zone was sampled using k -point densities of 2.5 \AA^{-1} and 5.0 \AA^{-1} for insulating and metallic systems, respectively. The Γ -point was sampled for the 3×3 supercells that were used for the point-defect calculations. For the band structure, the path in the reciprocal space was determined using seekpath.⁵²

The conjugated gradient algorithm was used to obtain the equilibrium atomic structures with the cutoff force of 0.005 eV \AA^{-1} . For the defect calculations, for which lattice parameters were kept fixed, the force and total energy convergence criteria were set to 0.03 eV \AA^{-1} and 10^{-5} eV, respectively. The dielectric tensors of the monolayer and the bilayer were computed through the self-consistent response to finite electric fields using the HSE+D3 hybrid functional. All the VASP input settings were generated using the VISE code (version 0.9.0).^{53,54}

4.2 Point-defect calculations

Point defects in the monolayer and the bilayer β -TeO₂ were modeled using a 3×3 supercell, with the slab thickness set to 20 \AA . The initial interstitial sites were identified by locating the charge density minima.⁵⁵ Initially, the PBEsol functional²¹ was used to screen for the

energetically favorable defects. The atomic positions of the prescreened defects were further relaxed using the HSE+D3 hybrid functional.

The defect formation energy (E_f) of defect D in charge state q was calculated as follows:^{17,56}

$$E_f = \{E[D^q] + E_{\text{corr}}[D^q]\} - E_P - \sum n_i \mu_i + q(\epsilon_{\text{VBM}} + \Delta\epsilon_F), \quad (2)$$

where $E[D^q]$ and E_P are the total energies of the defective and pristine supercells, respectively, and $E_{\text{corr}}[D^q]$ is the correction energy for the charged defect D^q under periodic boundary conditions (see Sec. 4.4). n_i is the number of atoms of element i added ($n_i > 0$) or removed ($n_i < 0$) to form the defect, μ_i is the chemical potential of that element, ϵ_{VBM} is the energy level of the VBM, and $\Delta\epsilon_F$ is the Fermi level with respect to the VBM.

4.3 Chemical potential diagram

The chemical potentials are constrained by competing phases under equilibrium conditions. The chemical potential diagram for the Te-O binary system, constructed from PBEsol total energies, is shown in Figure S2. The considered competing phases include Te ($P3_121$), TeO_2 ($Pbca$), Te_2O_5 ($P12_1\bar{1}$, $C12/m1$), and molecular O_2 in its triplet state. The TeO_2 phase is defined by points A ($\mu_{\text{O}} = -1.68$ eV; $\mu_{\text{Te}} = 0.00$ eV) and B ($\mu_{\text{O}} = -0.51$ eV; $\mu_{\text{Te}} = -2.36$ eV), representing Te-rich and O-rich conditions, respectively. A comprehensive list of phases, whose structures were sourced from the Materials Project Database (MPD),⁵⁷ along with the chemical potentials used in dopant calculations, is available in the *Supporting Information*. For defect formation energy calculations based on HSE+D3, the energy alignment accounts for the energy differences between the simple substances and the O_2 molecule, using PBEsol and HSE+D3.

4.4 Corrections on defect formation energies

The image-charge correction energy, $E_{\text{corr}}[D^q]$, was calculated following the correction scheme for two-dimensional systems proposed by Noh *et al.*⁵⁸ and Komsa *et al.*,³⁶ combined with the Sundararaman and Ping approach⁵⁹ for isolated Gaussian charges. Note that the correction method is an extension of the method proposed by Freysoldt *et al.*,⁶⁰ which is known to accurately correct the formation energy of defects in various materials.^{61–63} This was implemented using the PYDEFECT_2D code.⁶⁴ For this correction, the dielectric profiles of 2D β -TeO₂ were modeled using a step function. The thicknesses of the step-like dielectric profiles (w_z) were set to 5.3 Å for the monolayer and 11.5 Å for the bilayer, with edge smearing $\beta = 0.5$ Å.⁶⁴ Additionally, we employed PYDEFECT⁵⁴ to parse $E_{\text{corr}}[D^q]$, compute defect formation energies, and determine charge transition levels. Further details are available in the references.^{64,65}

4.5 Charge transition level

A transition level is defined as the Fermi level where the most stable charge state changes. Using the defect formation energies, the transition level $\epsilon(q/q')$ between charge states q and q' , where $\Delta E_f[D, q] = \Delta E_f[D, q']$, is calculated as:

$$\epsilon(q/q') = \frac{\Delta E_f[D, q'] - \Delta E_f[D, q]}{q - q'}. \quad (3)$$

When $q > q'$, charge state q is more stable for Fermi levels below $\epsilon(q/q')$, and vice versa. The Fermi levels are usually referenced relative to the VBM. The gap between $\epsilon(0/-1)$ and the VBM corresponds to the acceptor level, and the gap between $\epsilon(+1/0)$ and the CBM represents the donor level.

Supporting Information Available

The Supporting Information is available free of charge at <https://pubs.acs.org/doi/xxx>. A brief discussion on the Fermi level pinning by defects in 2D β -TeO₂; details on the evaluation of the STHs and calculations of β -TeO₂/SiO₂ interfaces; information on the PAW potentials used in this study; the chemical potentials and competing phases considered to build the chemical potential diagrams; top and side views of the monolayer and bilayer, together with their respective band structure and DOS; the chemical potential diagram for the TeO₂; formation energy diagrams for the native defects, obtained from PBEsol calculations; extended formation energy diagrams for the native defects, impurities, and dopants, obtained from HSE+D3 calculations; partial charge isosurfaces of the selected defect states in the monolayer and bilayer; charge density difference and their plane average along the c axis for the Al_{i3}³⁺ defect and β -TeO₂/SiO₂ interfaces, as well as the interface separation distance and the interface binding energies.

Acknowledgments

The authors thank the support from JSPS KAKENHI Grant Number 22H01755 and 23KF0030 and the E-IMR project at IMR, Tohoku University. Part of calculations were conducted using MASAMUNE-IMR (Project No. 202312-SCKXX-0408) and ISSP supercomputers.

References

- (1) Yoshikawa, A.; Matsunami, H.; Nanishi, Y. *Wide Bandgap Semiconductors*; Springer Berlin Heidelberg, 2007; p 1–24.
- (2) Shi, J.; Zhang, J.; Yang, L.; Qu, M.; Qi, D.; Zhang, K. H. L. Wide Bandgap Oxide Semiconductors: from Materials Physics to Optoelectronic Devices. *Adv. Mater.* **2021**, *33*, 2006230.

- (3) Majumder, S. B.; Jain, M.; Dobal, P. S.; Katiyar, R. S. Investigations on Solution Derived Aluminium Doped Zinc Oxide Thin Films. *Mater. Sci. Eng. B.* **2003**, *103*, 16–25.
- (4) Kim, D.; Lee, S. Persistent Metallic Sn-doped In₂O₃ Epitaxial Ultrathin Films with Enhanced Infrared Transmittance. *Sci. Rep.* **2020**, *10*, 4957.
- (5) Troughton, J.; Atkinson, D. Amorphous InGaZnO and Metal Oxide Semiconductor Devices: An Overview and Current Status. *J. Mater. Chem. C* **2019**, *7*, 12388–12414.
- (6) Hautier, G.; Miglio, A.; Ceder, G.; Rignanese, G.-M.; Gonze, X. Identification and design principles of low hole effective mass p-type transparent conducting oxides. *Nat. Commun.* **2013**, *4*, 2292.
- (7) Kumagai, Y. Computational Screening of *p*-Type Transparent Conducting Oxides Using the Optical Absorption Spectra and Oxygen-Vacancy Formation Energies. *Phys. Rev. Appl.* **2023**, *19*, 034063.
- (8) Gake, T.; Kumagai, Y.; Takahashi, A.; Oba, F. Point defects in *p*-type transparent conductive CuMO₂ (*M* = Al, Ga, In) from first principles. *Phys. Rev. Mater.* **2021**, *5*, 104602.
- (9) Guo, S.; Zhu, Z.; Hu, X.; Zhou, W.; Song, X.; Zhang, S.; Zhang, K.; Zeng, H. Ultra-thin Tellurium Dioxide: Emerging Direct Bandgap Semiconductor with High-mobility Transport Anisotropy. *Nanoscale* **2018**, *10*, 8397–8403.
- (10) Zavabeti, A. et al. High-mobility *p*-type Semiconducting Two-dimensional β -TeO₂. *Nat. Electron.* **2021**, *4*, 277–283.
- (11) Shi, J.; Sheng, Z.; Zhu, L.; Xu, X.; Gao, Y.; Tang, D.; Zhang, K. H. L. The Electronic Structure of β -TeO₂ as Wide Bandgap *p*-type Oxide Semiconductor. *Appl. Phys. Lett.* **2023**, *122*, 101901.

- (12) Yuan, Y.; Zhu, Z.; Zhao, S.; Li, W. Intrinsic Negative Poisson's Ratio of the Monolayer Semiconductor β -TeO₂. *J. Phys.: Condens. Matter* **2024**, *36*, 305301.
- (13) Biswas, R. K.; Pati, S. K. Achievement of Strain-driven Ultrahigh Carrier Mobility in β -TeO₂. *Mater. Res. Bull.* **2021**, *141*, 111343.
- (14) Dong, L.; Li, P.; Zhao, Y.; Miao, Y.; Peng, B.; Xin, B.; Liu, W. First-principles Study on the Electronic Properties of Layered Ga₂O₃/TeO₂ Heterolayers for High-performance Electronic Devices. *Appl. Surf. Sci.* **2022**, *602*, 154382.
- (15) Guo, S.; Qu, H.; Zhou, W.; Yang, S. A.; Ang, Y. S.; Lu, J.; Zeng, H.; Zhang, S. High-Performance and Low-Power Transistors Based on Anisotropic Monolayer β -TeO₂. *Phys. Rev. Appl.* **2022**, *17*, 064010.
- (16) Liu, A.; Kim, Y.-S.; Kim, M. G.; Reo, Y.; Zou, T.; Choi, T.; Bai, S.; Zhu, H.; Noh, Y.-Y. Selenium-alloyed Tellurium Oxide for Amorphous *p*-channel Transistors. *Nature* **2024**, *629*, 798–802.
- (17) Freysoldt, C.; Grabowski, B.; Hickel, T.; Neugebauer, J.; Kresse, G.; Janotti, A.; Van de Walle, C. G. First-principles Calculations for Point Defects in Solids. *Rev. Mod. Phys.* **2014**, *86*, 253–305.
- (18) Oba, F.; Kumagai, Y. Design and Exploration of Semiconductors from First Principles: A Review of Recent Advances. *Appl. Phys. Express* **2018**, *11*, 060101.
- (19) Huyen, V. T. N.; Bae, S.; Costa-Amaral, R.; Kumagai, Y. Native Defects and *p*-type Dopability in Transparent β -TeO₂: A First-principles Study. Accepted for publication in *Phys. Rev. Applied* on 3 October 2024.
- (20) Perdew, J. P.; Burke, K.; Ernzerhof, M. Generalized Gradient Approximation Made Simple. *Phys. Rev. Lett.* **1996**, *77*, 3865–3868.

- (21) Perdew, J. P.; Ruzsinszky, A.; Csonka, G. I.; Vydrov, O. A.; Scuseria, G. E.; Constantin, L. A.; Zhou, X.; Burke, K. Restoring the Density-Gradient Expansion for Exchange in Solids and Surfaces. *Phys. Rev. Lett.* **2008**, *100*, 136406.
- (22) Sun, J.; Ruzsinszky, A.; Perdew, J. P. Strongly Constrained and Appropriately Normed Semilocal Density Functional. *Phys. Rev. Lett.* **2015**, *115*, 036402.
- (23) Hui, K.; Chai, J.-D. SCAN-based Hybrid and Double-hybrid Density Functionals from Models without Fitted Parameters. *J. Chem. Phys.* **2016**, *144*, 044114.
- (24) Adamo, C.; Barone, V. Toward Reliable Density Functional Methods without Adjustable Parameters: The PBE0 Model. *J. Chem. Phys.* **1999**, *110*, 6158–6170.
- (25) Heyd, J.; Scuseria, G. E.; Ernzerhof, M. Hybrid Functionals Based on a Screened Coulomb Potential. *J. Chem. Phys.* **2003**, *118*, 8207–8215.
- (26) Krukau, A. V.; Vydrov, O. A.; Izmaylov, A. F.; Scuseria, G. E. Influence of the Exchange Screening Parameter on the Performance of Screened Hybrid Functionals. *J. Chem. Phys.* **2006**, *125*, 224106.
- (27) Schimka, L.; Harl, J.; Kresse, G. Improved Hybrid Functional for Solids: The HSEsol Functional. *J. Chem. Phys.* **2011**, *134*, 024116.
- (28) Grimme, S.; Antony, J.; Ehrlich, S.; Krieg, H. A Consistent and Accurate *Ab initio* Parametrization of Density Functional Dispersion Correction (DFT-D) for the 94 elements H-Pu. *J. Chem. Phys.* **2010**, *132*, 154104.
- (29) Beyer, H. Verfeinerung der Kristallstruktur von Tellurit, dem rhombischen TeO₂. *Z. Kristallogr. Cryst. Mater.* **1967**, *124*, 228–237.
- (30) Shannon, R. D. Revised Effective Ionic Radii and Systematic Studies of Interatomic Distances in Halides and Chalcogenides. *Acta Crystallogr. Sect. A* **1976**, *32*, 751–767.

- (31) Kumagai, Y.; Choi, M.; Nose, Y.; Oba, F. First-principles Study of Point Defects in Chalcopyrite ZnSnP₂. *Phys. Rev. B* **2014**, *90*, 125202.
- (32) Kumagai, Y.; Kavanagh, S. R.; Suzuki, I.; Omata, T.; Walsh, A.; Scanlon, D. O.; Morito, H. Alkali Mono-Pnictides: A New Class of Photovoltaic Materials by Element Mutation. *PRX Energy* **2023**, *2*, 043002.
- (33) Wang, D.; Han, D.; Li, X.-B.; Xie, S.-Y.; Chen, N.-K.; Tian, W. Q.; West, D.; Sun, H.-B.; Zhang, S. Determination of Formation and Ionization Energies of Charged Defects in Two-Dimensional Materials. *Phys. Rev. Lett.* **2015**, *114*, 196801.
- (34) Wang, D.; Han, D.; West, D.; Chen, N.-K.; Xie, S.-Y.; Tian, W. Q.; Meunier, V.; Zhang, S.; Li, X.-B. Excitation to Defect-bound Band Edge States in Two-dimensional Semiconductors and its Effect on Carrier Transport. *npj Comput. Mater.* **2019**, *5*, 8.
- (35) Ma, M.-Y.; Chen, N.-K.; Wang, D.; Han, D.; Sun, H.-B.; Zhang, S.; Li, X.-B. Defect Physics in 2D Monolayer I-VII Semiconductor AgI. *Mater. Today Nano* **2023**, *22*, 100304.
- (36) Komsa, H.-P.; Berseneva, N.; Krasheninnikov, A. V.; Nieminen, R. M. Charged Point Defects in the Flatland: Accurate Formation Energy Calculations in Two-dimensional Materials. *Phys. Rev. X* **2014**, *4*, 031044.
- (37) Sun, J.; Passacantando, M.; Palumbo, M.; Nardone, M.; Kaasbjerg, K.; Grillo, A.; Di Bartolomeo, A.; Caridad, J. M.; Camilli, L. Impact of Impurities on the Electrical Conduction of Anisotropic Two-Dimensional Materials. *Phys. Rev. Appl.* **2020**, *13*, 044063.
- (38) Wang, C.; Peng, L.; Wells, S. A.; Cain, J. D.; Huang, Y.-K.; Rhoads, L. A.; Dravid, V. P.; Hersam, M. C.; Grayson, M. A. Field-effect Conductivity Scaling for Two-dimensional Materials with Tunable Impurity Density. *2D Mater.* **2022**, *9*, 031002.

- (39) Bae, S.; Miyamoto, I.; Kiyohara, S.; Kumagai, Y. Universal polaronic behavior in elemental doping of MoS₂ from first principles. Accepted for publication in *ACS Nano* on 15 October 2024.
- (40) Wang, Q.; Shao, Y.; Shi, X. Mechanism of Charge Redistribution at the Metal–Semiconductor and Semiconductor–Semiconductor Interfaces of Metal–Bilayer MoS₂ Junctions. *J. Chem. Phys.* **2020**, *152*, 244701.
- (41) Wang, Y.; Zheng, Y.; Han, C.; Chen, W. Surface Charge Transfer Doping for Two-dimensional Semiconductor-based Electronic and Optoelectronic Devices. *Nano Res.* **2020**, *14*, 1682–1697.
- (42) Huang, J.; Kang, J. Defect and Doping Properties of Two-Dimensional PdSe₂. *J. Phys. Chem. C* **2022**, *126*, 20678–20685.
- (43) El Rassy, H.; Pierre, A. NMR and IR Spectroscopy of Silica Aerogels with Different Hydrophobic Characteristics. *J. Non-Cryst. Solids* **2005**, *351*, 1603–1610.
- (44) Schmidt, P.; Masse, S.; Laurent, G.; Slodczyk, A.; Le Bourhis, E.; Perrenoud, C.; Livage, J.; Fröhlich, F. Crystallographic and Structural Transformations of Sedimentary Chalcedony in Flint upon Heat Treatment. *J. Archaeol. Sci.* **2012**, *39*, 135–144.
- (45) Franchini, C.; Kresse, G.; Podloucky, R. Polaronic Hole Trapping in Doped BaBiO₃. *Phys. Rev. Lett.* **2009**, *102*, 256402.
- (46) Nishio, T.; Ahmad, J.; Uwe, H. Spectroscopic Observation of Bipolaronic Point Defects in Ba_{1-x}K_xBiO₃. *Phys. Rev. Lett.* **2005**, *95*, 176403.
- (47) Foyevtsova, K.; Khazraie, A.; Elfimov, I.; Sawatzky, G. A. Hybridization Effects and Bond Disproportionation in the Bismuth Perovskites. *Phys. Rev. B* **2015**, *91*, 121114(R).

- (48) Kang, J. Phonon-Assisted Hopping through Defect States in MoS₂: A Multiscale Simulation. *J. Phys. Chem. Lett.* **2020**, *11*, 3615–3622.
- (49) Blöchl, P. E. Projector Augmented-Wave Method. *Phys. Rev. B* **1994**, *50*, 17953–17979.
- (50) Kresse, G.; Joubert, D. From Ultrasoft Pseudopotentials to the Projector Augmented-Wave Method. *Phys. Rev. B* **1999**, *59*, 1758–1775.
- (51) Kresse, G.; Hafner, J. Ab Initio Molecular Dynamics for Open-Shell Transition Metals. *Phys. Rev. B* **1993**, *48*, 13115–13118.
- (52) Hinuma, Y.; Pizzi, G.; Kumagai, Y.; Oba, F.; Tanaka, I. Band structure diagram paths based on crystallography. *Comput. Mater. Sci.* **2017**, *128*, 140–184.
- (53) Kumagai, Y. The VASP Integrated Supporting Environment (VISE), <https://github.com/kumagai-group/vise>.
- (54) Kumagai, Y.; Tsunoda, N.; Takahashi, A.; Oba, F. Insights into Oxygen Vacancies from High-throughput First-principles Calculations. *Phys. Rev. Materials* **2021**, *5*, 123803.
- (55) Tsunoda, N.; Kumagai, Y.; Oba, F. Recommendation of interstitial hydrogen positions in metal oxides. *Comput. Mater. Sci.* **2022**, *203*, 111068.
- (56) Kumagai, Y.; Oba, F. Electrostatics-based finite-size corrections for first-principles point defect calculations. *Phys. Rev. B* **2014**, *89*, 195205.
- (57) Jain, A.; Ong, S. P.; Hautier, G.; Chen, W.; Richards, W. D.; Dacek, S.; Cholia, S.; Gunter, D.; Skinner, D.; Ceder, G.; Persson, K. A. Commentary: The Materials Project: A Materials Genome Approach to Accelerating Materials Innovation. *APL Materials* **2013**, *1*, 011002.
- (58) Noh, J.-Y.; Kim, H.; Kim, Y.-S. Stability and Electronic Structures of Native Defects in Single-layer MoS₂. *Phys. Rev. B* **2014**, *89*, 205417.

- (59) Sundararaman, R.; Ping, Y. First-principles Electrostatic Potentials for Reliable Alignment at Interfaces and Defects. *J. Chem. Phys.* **2017**, *146*, 104109.
- (60) Freysoldt, C.; Neugebauer, J.; Van de Walle, C. G. Fully Ab Initio Finite-Size Corrections for Charged-Defect Supercell Calculations. *Phys. Rev. Lett.* **2009**, *102*, 016402.
- (61) Kumagai, Y.; Burton, L. A.; Walsh, A.; Oba, F. Electronic Structure and Defect Physics of Tin Sulfides: SnS, Sn₂S₃, and SnS₂. *Phys. Rev. Applied* **2016**, *6*, 014009.
- (62) Kumagai, Y.; Tsunoda, N.; Oba, F. Point Defects and *p*-Type Doping in ScN from First Principles. *Phys. Rev. Appl.* **2018**, *9*, 034019.
- (63) Tsunoda, N.; Kumagai, Y.; Takahashi, A.; Oba, F. Electrically Benign Defect Behavior in Zinc Tin Nitride Revealed from First Principles. *Phys. Rev. Appl.* **2018**, *10*, 011001.
- (64) Kumagai, Y. Corrections on Formation Energies and Eigenvalues of Point Defect Calculations in Two-dimensional Materials. *Phys. Rev. B* **2024**, *109*, 054106.
- (65) Kumagai, Y. PYDEFECT, <https://kumagai-group.github.io/pydefect>.